Spin wave propagation in a strain-controlled magnonic crystal with a piezoelectric layer

© A.A. Grachev, A.V. Sadovnikov

Saratov National Research State University,
Saratov, Russia

E-mail: stig133@gmail.com

The mechanisms of spin wave propagation in a magnonic-crystalline structure, which is a width-modulated magnetic microwaveguide loaded with a piezoelectric layer with a system of counter-pin electrodes, are considered. Computational modelling based on the finite element method has been used to estimate the transformation of the internal magnetic field in a magnonic crystal under the action of elastic deformations. The shift of the frequency band of the Bragg resonance and the depth of regression of the spin-wave signal at the frequency of the Bragg resonance when an electric potential is applied to the electrodes are observed. It is shown that changing the polarity of the electric field can effectively control the characteristics of the propagating spin waves and the spatial distribution of the dynamic magnetization intensity in the multiferroic structure.

1. Introduction

The main idea of magnonics [1,2] is in the use of spin waves (SW) or magnons as data signals for micro- and nanostructures [3] based on magnetic-ordered materials. The use of spin current carriers will allow to create next generation electronic devices [4] with considerable improvement of such parameters as data rate and power consumption by reducing the spatial dimensions of components. Spin-wave devices running in the frequency range from units of gigahertz to 10 THz and have a SW length which is four to five orders less than the radio waves of the same frequency, therefore they can be well integrated into modern micro- and nanoscale electronic devices [1,5,6]. Currently, yttrium-iron garnet (YIG) is a magnetic material with the lowest SW damping parameter [7]. Moreover, YIG is one of the most promising materials also due to the possibility to create nanoscale structures and low energy consumption during SW propagation. This opens wide opportunities for the use of such structures in nonvolatile memory [8], magnon transistors [9], magnon logics [10] and controlled microwave devices based on dielectric magnonics concepts [11].

Its is important that one of the SW propagation control mechanisms is the action of elastic deformation on magnetic structures [12–15]. This effect may be observed when magnetostriction film (e.g. YIG) is placed on a piezoelectric substrate — for example, lead zirconate titanate (LZT) [14,16,17]. Deformation of a piezoelectric substrate induced by an electric field is transferred to ferrite film whose internal magnetic field strength in the YIG layer is modulated by magnetostriction. Composite multiferroic structures composed of the YIG film and piezoelectric layer appear to allow SW spectrum control using both magnetic and electric field variations [16,17]. Magnon-crystal structures are functionally more flexible and have higher capabilities of controlling linear and non-linear characteristics than regular spin waveguides [18–20]. Therefore, currently the spin dynamics effects in magnon crystals are extensively studied due to their ability to be used as a basis for creation a wide range of data recording, storage and processing units. Regular waveguides with periodic width variation are much more difficult for study due to inhomogeneous internal static fields [21–23]. In addition, these studies addressed the possibility of SW spectrum control by adding a ferroelectric layer or arrangement of conductors with current along the film edges [21,22].

This study uses numerical and experimental investigations to demonstrate the SW spectra control effect by an electric field in a variable-width magnetic microwaveguide with a piezoelectric layer. Based on the finite element method, the effect of distributed elastic deformations on the internal magnetic field strength in a magnonic crystal is evaluated. Using time-domain micromagnetic calculations, amplitude-frequency characteristics of a multiferroic structure were obtained and frequency shift of the Bragg band gap was shown when the external electric field is varied.

2. Structure and numerical study

The studied structure is shown in Figure 1, a — is a microwaveguide formed from the YIG film ($Y_3Fe_5O_{12}$) $10\,\mu$m in thickness and $1\,$mm in width. The YIG film
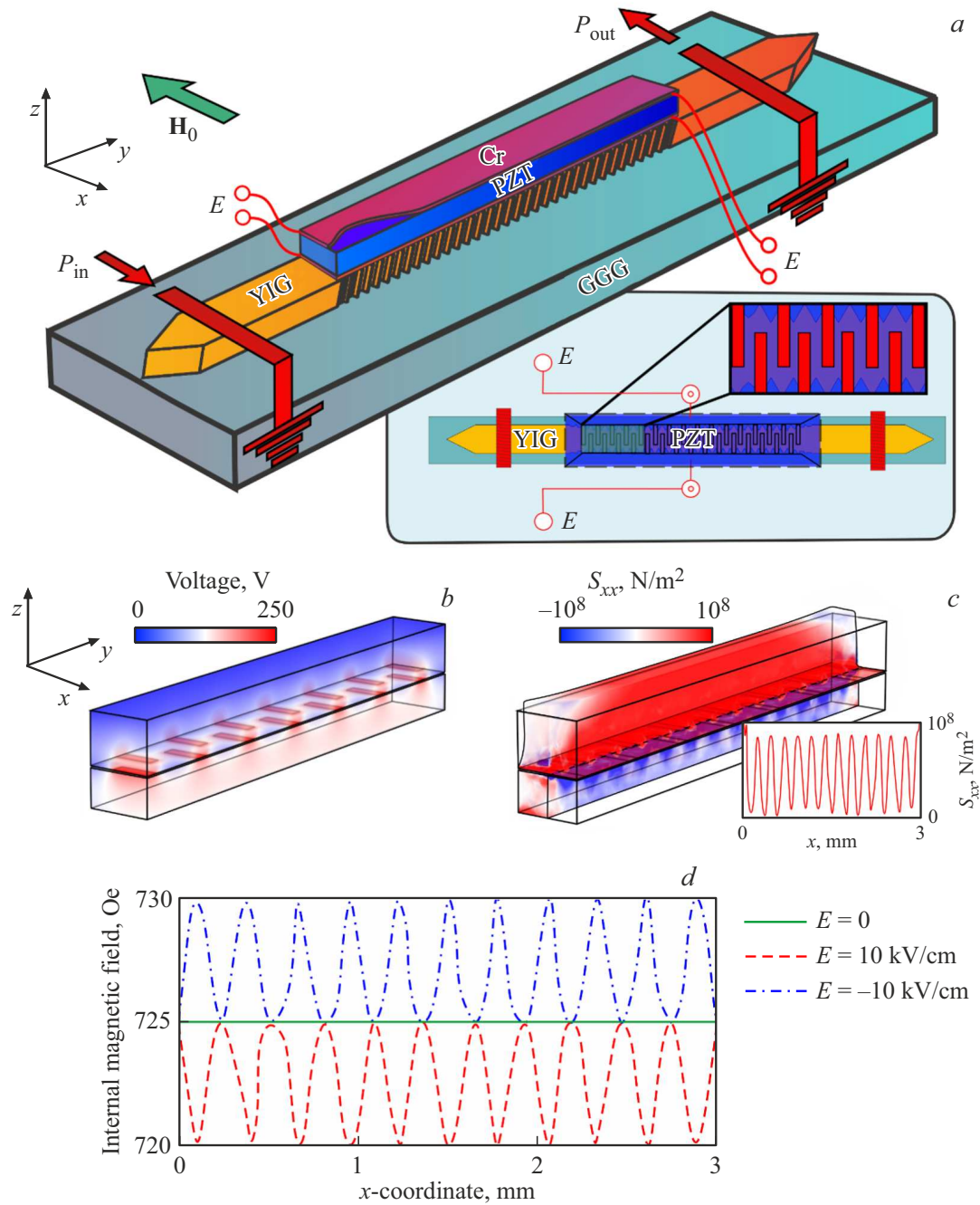
Figure 1. *a*) Diagram of the studied structure consisting of an irregular YIG waveguide with a piezoelectric layer. Detail in the right bottom corner: connection diagram of the electrode system to the LZT layer. *b*) Distribution of electrostatic potential when voltage is applied to the electrodes. *c*) Distribution of S_{xx} component of mechanical voltages when positive voltage is applied to the electrodes. *d*) Distributions of the internal magnetic field $|H_{int}(x)|$ along the magnon crystal length at different external electric field strengths $E = 0 \, \text{kV/cm}$ (green solid line), $E = 10 \, \text{kV/cm}$ (red dashed curve) and $E = -10 \, \text{kV/cm}$ (blue dashed-dotted curve).

was grown by the liquid-phase epitaxy method on the gadolinium-gallium garnet substrate (GGG, $Gd_3Ga_5O_{12}$ (111)) $500 \, \mu\text{m}$ in thickness. YIG layer saturation magnetization is $4\pi M_0 = 1750 \, \text{G}$. The magnetic microwaveguide length is $L = 10 \, \text{mm}$. In the central segment 7 mm in length, the waveguide width was modulated using precision cutting of triangular regions with a period of $d = 250 \, \mu\text{m}$

to a depth of $200 \, \mu\text{m}$. As a result, a magnon crystal in the form of a waveguide with periodic width modulation and a regular waveguide section width of $600 \, \mu\text{m}$ was formed. A piezoelectric lead zirconate titanate layer (PZT, $Pb(Zr_{0.3}Ti_{0.7})O_3$) with dimensions $1000 \times 7000 \times 200 \, \mu\text{m}$ is applied on top of the magnon crystal. A titanium electrode 100 nm in thickness was sputtered on bottom of

the LZT layer, and a „interdigital" type electrode system was formed using a laser scribing method. The system coincided with the triangular region period of the magnon crystal; the increased multiferroic structure region is shown in the detail in Figure 1, a. A chromium electrode $1\,\mu m$ in thickness was sputtered on top of the LZT layer and has not significant effect on the SW propagation in the magnon crystal. For the experimental study, the magnon crystal was attached to the LZT layer using OMEGA TT300 2-part strain gage epoxy adhesive based on ethyl cyanoacrylate $C_6H_7NO_2$.

SW was induced using a microstrip transmission line with a microwave transducer $30\,\mu m$ in width and $2\,mm$ in length. The output transducer is at $9\,mm$ from the input transducer. The structure was placed in a uniform static magnetic field $H_0 = 730\,Oe$ oriented along the x axis for efficient excitation of magnetostatic surface waves (MSSW).

At the first stage, the amount of elastic deformation in the piezoelectric layer when positive or negative voltage is applied to the periodic system of electrodes shall be estimated quantitatively. For this a numerical model was developed on the basis of the finite element method [24,25]. First, elastic deformations caused by an external electric field in the piezoelectric layer were calculated. Next, the internal magnetic field profiles in the magnon crystal were calculated. The obtained internal magnetic field profiles were then used in micromagnetic simulations [26].

Figure 1, c shows the distribution of S_{xx} component of mechanical stresses when positive voltage is applied to the electrodes. Electrostatic potential distribution for this case is shown in Figure 1, b. These pictures show the findings for the central part of the magnon crystal $3\,mm$ in length. It can be seen that the piezoelectric layer deformation occurs near the electrodes and is transferred to the YIG film. The detail in Figure 1, c shows the distribution of S_{xx} component of mechanical stresses along the magnon crystal length and it can be suggested that the electrode system, when positive voltage is applied, induces periodic distribution of mechanical deformations along the piezoelectric layer length and, therefore, the YIG film.

Then, the influence of the piezoelectric layer deformation on the internal magnetic field of the magnon crystal was estimated, because the internal magnetic field varies due to the converse magnetostriction effect in the magnon crystal. The following magnetostriction constants for the YIG film at room temperature were used in the corresponding calculations: $\lambda_{100} = -1.4 \cdot 10^{-6}$ and $\lambda_{111} = -2.4 \cdot 10^{-6}$ equal to relative magnetostriction elongations along the corresponding x and z axes. Figure 1, d shows distributions of the internal magnetic field $|H_{\text{int}}(x)|$ along the magnon crystal length (along the y axis) at the external electric field strength $E = 0\,kV/cm$ (gree solid line), $E = 10\,kV/cm$ (red dashed curve) and $E = -10\,kV/cm$ (blue dashed-dotted curve). It should be noted that creation of waveguide modulation width already results in periodic potential of the internal magnetic field, but the amount of these modulations

in the mid-width of the magnon crystal is about $0.3\,Oe$, therefore $E = 0\,kV/cm$ (green solid line) in Figure 1, d corresponds to the straight line. It should be noted that the LZT layer is also a ferroelectric material (permittivity is $\varepsilon \approx 2000$) and, when a load is applied to the YIG film, hybrid electromagnetic spin waves are generated and influence the SW dispersion on the magnon crystal. For the study, the effect of elastic deformations on the spin wave spectrum is considered. When positive (red dashed curve in Figure 1, d) or negative (blue dashed-dotted curve in Figure 1, d) voltage is applied to the electrode system, the periodic potential of distributed elastic deformations is transferred to the magnon crystal and forms non-uniform distribution of the internal magnetic field along the magnon crystal which coincides with the period of etched triangular regions on the YIG microwaveguide. Application of positive electric field results in the reduction of internal magnetic field $|H_{\text{int}}(x)|$, while application of negative electric field results in an increase of $|H_{\text{int}}(x)|$. This result will be further used in the calculation of SW transmission spectra in the magnon crystal during micromagnetic simulation.

Since now the variations of the static distribution of the magnetic field in the magnon crystal exposed to elastic deformations are known, proceed to a dynamic problem of SW generation and propagation in the studied system. For this, micromagnetic simulation by the finite-difference time domain method was used. Free software code mumax[3] supporting CUDA parallel computing technology was used. This method is based on the numerical solution of the Landau−Lifshitz−-Gilbert (LLG) equation [26]:

$$\frac{\partial \mathbf{M}}{\partial t} = \gamma[\mathbf{H}_{\text{eff}}\mathbf{M}] + \frac{\alpha}{M_0}\left[\mathbf{M}\,\frac{\partial \mathbf{M}}{\partial t}\right],$$

where $\mathbf{M}$ — is the magnetization vector, $\alpha = 10^{-5}$ is the damping parameter phenomenologically introduced by Gilbert,

$$\mathbf{H}_{\text{eff}} = \mathbf{H}_0 + \mathbf{H}_{\text{demag}} + \mathbf{H}_{\text{ex}} + \mathbf{H}_a(E)$$

is the effective magnetic field, $\mathbf{H}_0$ is external magnetic field, $\mathbf{H}_{\text{demag}}$ is the demagnetization field, $\mathbf{H}_{\text{ex}}$ is the exchange field, $\mathbf{H}_a(E)$ is the anisotropy field, including the external electric field, $\gamma = 2.8\,MHz/Oe$ is the gyromagnetic ratio in the YIG film. Exchange constant in the YIG film is equal to $A_{\text{ex}} = 3.612\,pJ/m$. To reduce the signal reflection from the computational domain boundaries ($y = 0$ and $y = 10\,mm$), domains ($0 < y < 0.5\,mm$ and $9.5 < y < 10\,mm$) with geometrically increasing coefficient α were introduced. The mesh size was set to $5 \times 5 \times 1\,\mu m^3$ to avoid the influence of non-uniform exchange.

Spectral density of the output signal $P(f)$ was calculated along the x axis in cross-section $y = 7\,mm$ corresponding to the output antenna domain designated as P_{out} in Figure 1, a. For this, the input signal was written as $h_z(t) = h_0 \text{sinc}(2\pi f_c t)$, where the carrier frequency $f_c = 7\,GHz$, $h_0 = 0.1\,Oe$. Then the dynamic magnetization
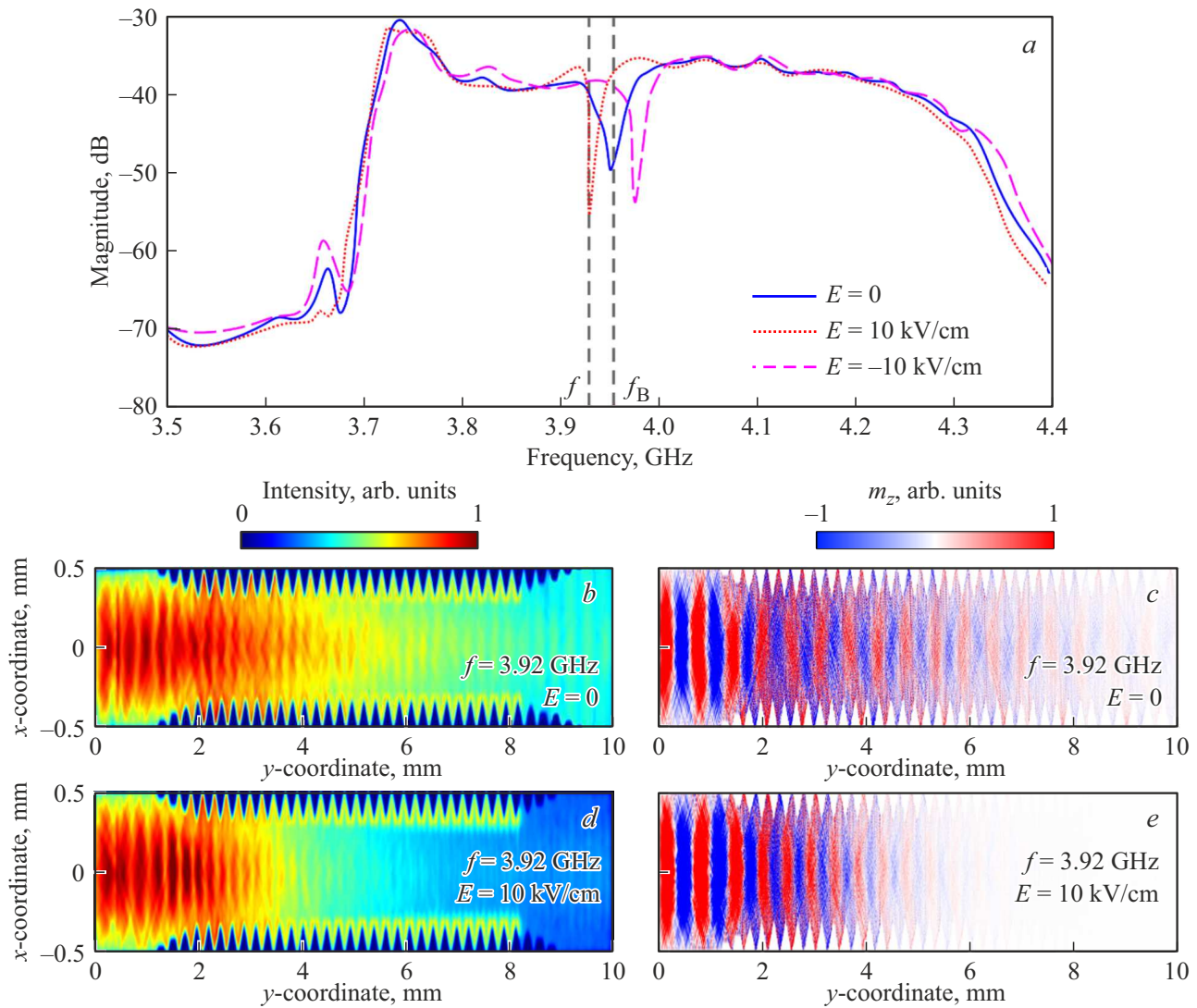
Figure 2. a) Frequency dependences of the spectral density of the output signal power $P(f)$ for different external electric field strengths calculated using micromagnetic simulation. $b-e$) Micromagnetic simulation of spin wave intensity distribution (b, d) and magnetization component distribution of dynamic m_z (c, e) for various external electric field strengths. Input signal frequency is $f = 3.92$ GHz.

$m_z(x, y, t)$ in the output section domain P_{out} was written with step $\Delta t = 75$ fs during $T = 500$ ns. As a result, it was possible to plot a frequency dependence of dynamic magnetization at the output $P_{out}(f)$ using the Fourier double transformation.

Figure 2, a shows the distribution of spectral power density in the output section of the magnon crystal corresponding to spin wave transmission when the external electric field applied to the piezoelectric layer is varied. The blue curve in Figure 2, a plotted for $E = 0$ kV/cm demonstrates a strongly pronounced Bragg band gap with the carrier frequency of $f_B = 3.95$ GHz and width of $\Delta f = 15$ MHz in the SW transmission spectrum. Application of the positive electric field (red curve in Figure 2, a) displaces the SW dispersion curve into the low frequency domain and, therefore, shifts the Bragg band gap to the low frequency domain, and application of the negative electric field (pink curve in Figure 2, a) moves the Bragg band gap to the high frequency domain. Whilst both width Δf and depth ΔS of the Bragg band gap are varied due to the transformation of the internal magnetic field. It should be also noted that provision of additional periodicity by the internal magnetic field results in increasing power dip depth in the Bragg band gap domain.

Note that the effect of elastic deformations on the SW spectrum results in the transformation of spatial distribution of dynamic magnetization in the magnon crystal. Figure 2, $b-e$ shows the micromagnetic simulation of spin wave intensity distribution (see Figure 2, b and d) proportional to the squared dynamic magnetization $I(x, y) = m_y^2 + m_z^2$ and distribution of magnetization component of dynamic m_z (see Figure 2, c and e) at the input frequency $f = 3.92$ GHz corresponding to the SW transmission conditions in the magnon crystal at
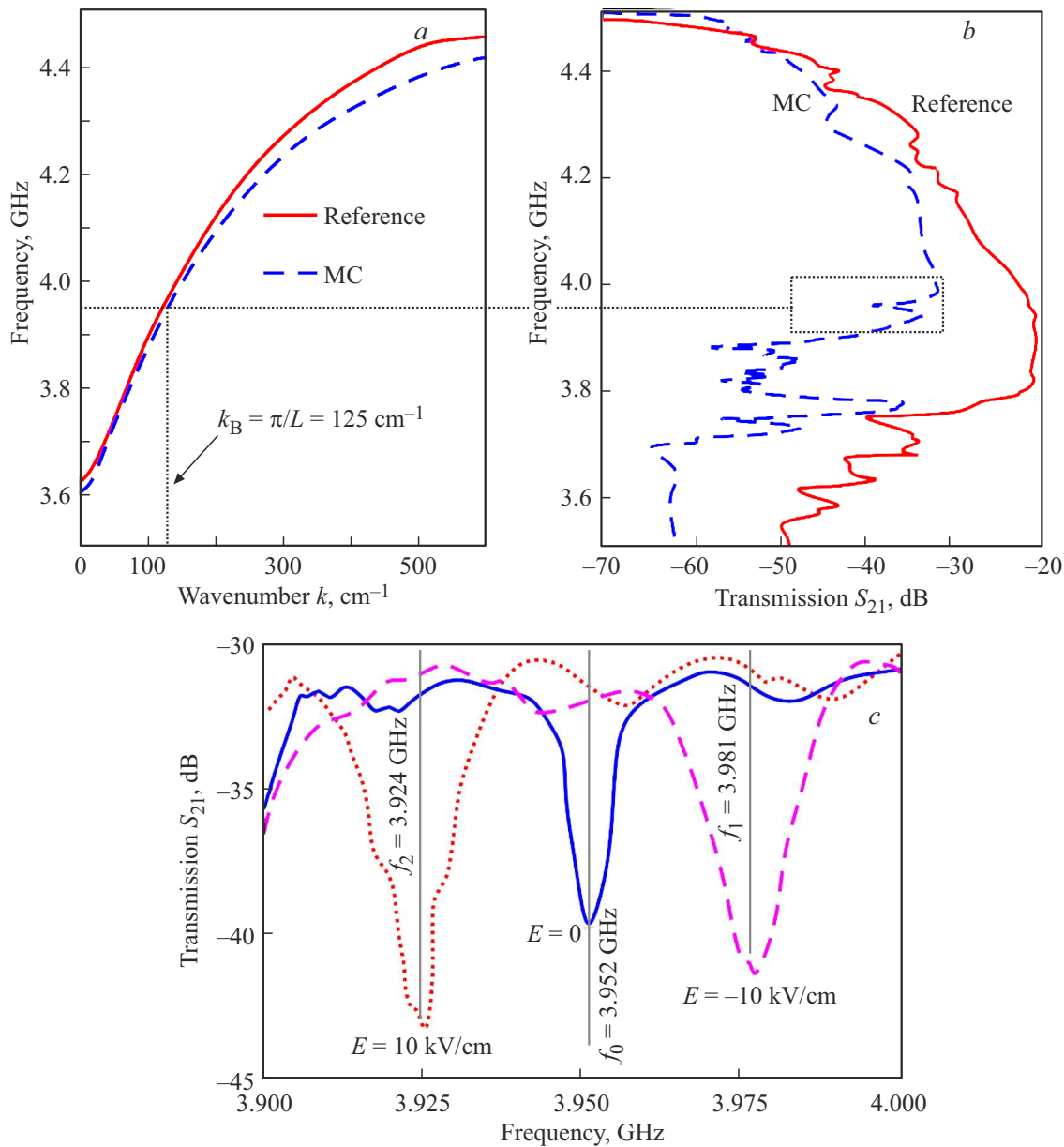
Figure 3. a) Dispersion characteristics of MSSW and b) AFC of transmission coefficient (S_{21}) of SW propagating in a regular magnetic microwaveguide (red solid lines) and magnon crystal (blue dashed curves) measured using the vector circuit analyzer. c) AFC of transmission coefficient (S_{21}) of SW propagating in the magnon crystal with $E = 0$ kV/cm (blue solid curve), $E = 10$ kV/cm (red dotted curve) and $E = -10$ kV/cm (pink dashed curve).

$E = 0$ kV/cm (Figure 2, b and c). When the external electric field is applied $E = 10$ kV/cm (see Figure 2, d and e), the Bragg band gap position is shifted to the low frequency domain and SW damping in the magnon crystal is observed on the spatial distributions in the Bragg band gap frequency domain.

3. Experimental study

   Using radiophysical measurements conducted on E8362C PNA vector circuit analyzer, dispersion (see

Figure 3, a) and amplitude-frequency characteristics (AFC) were measured (see Figure 3, b) of the transmission coefficient (S_{21}) of MSSW for the regular magnetic microwaveguide (red solid curve) 1 mm in width and magnon crystal with piezoelectric layer (blue dashed curve). Blue solid curve in Figure 3, b shows the measured AFC for MSSW in case of external electric field $E = 0$ kV/cm. It can be seen that a distinctive MSSW power dip is formed on AFC which is associated with the Bragg band gap in the magnon crystal. The frequency corresponds to the Bragg wave number $k_B = \pi/d$. The band gap frequency width is $\Delta f = 10$ MHz at -40 dB. To ensure that the frequency do-

main corresponds to the central frequency of the Bragg band gap, MSSW dispersion (see Figure 3, a) in the magnon crystal was measured. Then thanks to the positive value of the applied electric field (see the red dashed line in Figure 3, c), frequency displacement of the SW dispersion curve takes place and, therefore, the band gap position also shifts to 28 MHz (carrier frequencies of the Bragg band gaps are shown in Figures 3, c). When the negative electric field is applied (see the pink dashed curve in Figure 3, c), the band gap is shifted to the low frequency domain. This effect is explained by the decreasing internal magnetic field in case of positive polarity and decreasing external electric field in case of negative polarity as shown by the numerical simulation. Note that the effect of elastic deformations on the magnon crystal results not only in frequency shift of the band gap, but also to the variation of its width (Δf) and depth (ΔS).

4. Conclusion

Therefore, spin wave distribution mechanisms were investigated in the magnon-crystal structure which is composed of the variable-width magnetic microwaveguide loaded with a piezoelectric layer with the metal electrode grid whose period matches the magnon crystal period. Using the finite element simulation, internal magnetic field transformation was estimated in the magnon crystal due to elastic deformations induced by the application of potential to the electrodes. It is shown that potential applied to the „interdigital" system results in two effects. First, to the variation of the averaged internal effective field strength in MC followed by frequency shift of the Bragg resonance band „up" or „down" depending on the sign of the electric potential. Second, the spin wave signal rejection depth at the Bragg resonance frequency at sufficiently large, but experimentally implemented electric field strengths on electrodes increases due to the increase in the internal effective field modulation depth in case of deformations. The offered method allows effective control of the propagating spin waves and spatial distribution of the dynamic magnetization intensity in the multiferroic structure.

Funding

Conflict of interest

The authors declare that they have no conflict of interest.

References

[1] A. Barman, G. Gubbiotti, S. Ladak, A.O. Adeyeye, M. Krawczyk, J. Gräfe, C. Adelmann, S. Cotofana, A. Naeemi, V.I. Vasyuchka, B. Hillebrands, S.A. Nikitov, H. Yu, D. Grundler, A.V. Sadovnikov, A.A. Grachev, S.E. Sheshukova, J.-Y. Duquesne, M. Marangolo, G. Csaba, W. Porod, V.E. Demidov, S. Urazhdin, S.O. Demokritov, E. Albisetti, D. Petti, R. Bertacco, H. Schultheiss, V.V. Kruglyak, V.D. Poimanov, S. Sahoo, J. Sinha, H. Yang, M. Münzenberg, T. Moriyama, S. Mizukami, P. Landeros, R.A. Gallardo, G. Carlotti, J.-V. Kim, R.L. Stamps, R.E. Camley, B. Rana, Y. Otani, W. Yu, T. Yu, G.E.W. Bauer, C. Back, G.S. Uhrig, O.V. Dobrovolskiy, B. Budinska, H. Qin, S. van Dijken, A.V. Chumak, A. Khitun, D.E. Nikonov, I.A. Young, B.W. Zingsem, M. Winklhofer. J. Phys.: Condens. Matter **33**, *41*, 413001 (2021).

[2] V.V. Kruglyak, S.O. Demokritov, D. Grundler. J. Phys. D **43**, *26*, 264001 (2010).

[3] Q. Wang, M. Kewenig, M. Schneider, R. Verba, F. Kohl, B. Heinz, M. Geilen, M. Mohseni, B. Lägel, F. Ciubotaru, C. Adelmann, C. Dubs, S.D. Cotofana, O.V. Dobrovolskiy, T. Brächer, P. Pirro, A.V. Chumak. Nature Electron. **3**, *12*, 765 (2020).

[4] S. Bader, S. Parkin. Annu. Rev. Condens. Matter Phys. **1**, 71 (2010).

[5] A. Mahmoud, F. Ciubotaru, F. Vanderveken, A.V. Chumak, S. Hamdioui, C. Adelmann, S. Cotofana. J. Appl. Phys. **128**, *16*, 161101 (2020).

[6] A. Chumak, P. Kabos, M. Wu, C. Abert, C. Adelmann, A. Adeyeye, J. Åkerman, F. Aliev, A. Anane, A. Awad, C.H. Back, A. Barman, G.E.W. Bauer, M. Becerer, E.N. Beginin, V.A.S.V. Bittencourt, Y.M. Blanter, P. Bortolotti, I. Boventer, D.A. Bozhko, S.A. Bunyaev, J.J. Carmiggelt, R.R. Cheenikundil, F. Ciubotaru, S. Cotofana, G. Csaba, O.V. Dobrovolskiy, C. Dubs, M. Elyasi, K.G. Fripp, H. Fulara, I.A. Golovchanskiy, C. Gonzalez-Ballestero, P. Graczyk, D. Grundler, P. Gruszecki, G. Gubbiotti, K. Guslienko, A. Haldar, S. Hamdioui, R. Hertel, B. Hillebrands, T. Hioki, A. Houshang, C.-M. Hu, H. Huebl, M. Huth, E. Iacocca, M.B. Jungfleisch, G.N. Kakazei, A. Khitun, R. Khymyn, T. Kikkawa, M. Kläui, O. Klein, J.W. Kłos, S. Knauer, S. Koraltan, M. Kostylev, M. Krawczyk, I.N. Krivorotov, V.V. Kruglyak, D. Lachance-Quirion, S. Ladak, R. Lebrun, Y. Li, M. Lindner, R. Macêdo, S. Mayr, G.A. Melkov, S. Mieszczak, Y. Nakamura, H.T. Nembach, A.A. Nikitin, S.A. Nikitov, V. Novosad, J.A. Otálora, Y. Otani, A. Papp, B. Pigeau, P. Pirro, W. Porod, F. Porrati, H. Qin, B. Rana, T. Reimann, F. Riente, O. Romero-Isart, A. Ross, A.V. Sadovnikov, A.R. Safin, E. Saitoh, G. Schmidt, H. Schultheiss, K. Schultheiss, A.A. Serga, S. Sharma, J.M. Shaw, D. Suess, O. Surzhenko, K. Szulc, T. Taniguchi, M. Urbánek, K. Usami, A.B. Ustinov, T. van der Sar, S. van Dijken, V.I. Vasyuchka, R. Verba, S. Viola Kusminskiy, Q. Wang, M. Weides, M. Weiler, S. Wintz, S.P. Wolski, X. Zhang. IEEE Trans. Magn. **58**, *6*, 0800172 (2022).

[7] D.D. Stancil, A. Prabhakar. Spin Waves: Theory and Applications. Springer Science & Business Media (2009).

[8] A. Khitun, K.L. Wang. J. Appl. Phys. **110**, *3*, 034306 (2011).

[9] K. Das, F. Feringa, M. Middelkamp, B. Van Wees, I.J. Vera-Marun. Phys. Rev. B **101**, *5*, 054436 (2020).

[10] Q. Wang, A.V. Chumak, P. Pirro. Nature Commun. **12**, 2636 (2021).

[11] S.A. Nikitov, A.R. Safin, D.V. Kalyabin, A.V. Sadovnikov, E.N. Beginin, M.V. Logunov, M.A. Morozova, S.A. Odintsov, S.A. Osokin, A.Yu. Sharaevskaya, Yu.P. Sharaevsky, A.I. Kirilyuk. Phys.−Usp. **63**, *10*, 945 (2020).

[12] A.A. Bukharaev, A.K. Zvezdin, A.P. Pyatakov, Y.K. Fetisov. Phys.−Usp. **61**, *5*, 1175 (2018).

[13] B. Rana, Y. Otani. Commun. Phys. **2**, 90 (2019).

[14] A.V. Sadovnikov, A.A. Grachev, S.E. Sheshukova, Yu.P. Shara-evskii, A.A. Serdobintsev, D.M. Mitin, S.A. Nikitov. Phys. Rev. Lett. **120**, *25*, 257203 (2018).

[15] S. Bandyopadhyay, J. Atulasimha, A. Barman. Appl. Phys. Rev. **8**, *4*, 041323 (2021).

[16] A. Grachev, O. Matveev, M. Mruczkiewicz, M. Morozova, E. Beginin, S. Sheshukova, A. Sadovnikov. Appl. Phys. Lett. **118**, *26*, 262405 (2021).

[17] A.A. Grachev, A.V. Sadovnikov, S.A. Nikitov. Nanomater. **12**, *9*, 1520 (2022).

[18] S.A. Nikitov, P. Tailhades, C.S. Tsai. J. Magn. Magn. Mater. **236**, *3*, 320 (2001).

[19] Yu.V. Gulyaev, S.A. Nikitov, L.V. Zhivotovskii, A.A. Klimov, Ph. Tailhades, L. Presmanes, C. Bonningue, C.S. Tsai, S.L. Vy-sotskii, Yu.A. Filimonov. JETP Lett. **77**, *10*, 567 (2003).

[20] S.L. Vysotskii, S.A. Nikitov, Yu.A. Filimonov. JETP **101**, *3*, 547 (2005).

[21] A.B. Ustinov, B.A. Kalinikos. Technical Phys. Lett. **40**, *7*, 568 (2014).

[22] A.A. Nikitin, A.B. Ustinov, A.A. Semenov, A.V. Chumak, A.A. Serga, V.I. Vasyuchka, E. Lähderanta, B.A. Kalinikos, B. Hillebrands. Appl. Phys. Lett. **106**, *10*, 102405 (2015).

[23] P. Frey, A.A. Nikitin, D.A. Bozhko, S.A. Bunyaev, G.N. Kaka-zei, A.B. Ustinov, B.A. Kalinikos, F. Ciubotaru, A.V. Chumak, Q. Wang, V.S. Tiberkevich, B. Hillebrands, A.A. Serga. Commun. Phys. **3**, *1*, 17 (2020).

[24] P.P. Silvester, R.L. Ferrari. Finite Elements for Electrical Engineers. Cambridge University Press (1996). 541 p.

[25] O.C. Zienkiewicz, R.L. Taylor, J.Z. Zhu. The Finite Element Method: Its Basis and Fundamentals. Elsevier (2005).

[26] A. Vansteenkiste, J. Leliaert, M. Dvornik, M. Helsen, F. Garcia-Sanchez, B. Van Waeyenberge. AIP Advances **4**, *10*, 107133 (2014).

Translated by Ego Translating